Role of hydroxyl groups of Zn-containing nanosized MFI zeolite for the photocatalytic oxidation of methane at room temperature in water

Diógenes Piva, Geqian Fang, Sajjad Ghojavand, Francesco Dalena, Nour Alhajjar, Vincent de Waele, Vitaly Ordomsky, Andrei Khodakov, Karima Ben Tayeb, Tiago Fernandes, et al.

Role of hydroxyl groups of Zn-containing nanosized MFI zeolite for the photocatalytic oxidation of methane at room temperature in water

Diógenes Honorato Piva[a], Sajjad Ghojavand[a], Francesco Dalena[a], Vincent De Waele[b], Geqian Fang[c], Vitaly Ordomsky[c], Andrei Khodakov[c], Tiago Fernandes[d], Yury V. Kolen'ko[d], Svetlana Mintova[a]*

[a] *Laboratoire Catalyse et Spectrochimie (LCS), Normandie Univ, ENSICAEN, UNICAEN, CNRS, 14000, Caen, France.*
[b] *Laboratoire de Spectroscopie pour les Interactions, la Réactivité et l'Environnement – LASIRE, Université de Lille, CNRS, UMR 8516, F-59000 Lille, France.*
[c] *Unité de Catalyse et Chimie du Solide - UCCS, Université Lille, CNRS, 59000 Lille, France.*
[d] *Nanochemistry Research Group, International Iberian Nanotechnology Laboratory (INL), Braga 4715-330, Portugal.*
* *svetlana.mintova@ensicaen.fr*

Abstract

Effective conversion of methane to a mixture of more valuable hydrocarbons and hydrogen under mild conditions is a great scientific and practical challenge. Here, we synthesized Zn-containing nanosized MFI zeolite for direct oxidation of methane in water using only oxygen as the oxidant under mild light irradiation at room temperature. The formation of the surface hydroxyl groups on nanosized MFI-type zeolite and their disappearance in the Zn-containing nanosized MFI zeolite were confirmed with infrared Fourier transform (FTIR) spectroscopy. Incorporation of atomically dispersed zinc atoms into the framework of nanosized MFI zeolite is revealed by Nuclear Magnetic Resonance and X-ray Photoelectron Spectroscopy. Unexpectedly, pure silica MFI zeolite exhibited the highest photocatalytic performance. Our finds demonstrated that large number of isolated silanol groups and silanol nests enhanced productivity of oxygenate compounds and C_2H_6, while the Zn incorporated into the zeolite framework or attached to the silanol nests of the nanosized zeolites are less efficient. A mechanism of photocatalytic methane oxidation is proposed. These findings provide insights into developing active nanosized zeolite photocatalysts with extended amount of surface hydroxyl groups that can play a key role in photocatalytic methane conversion.

Keywords: Photocatalytic conversion; nanosized zeolites; hydroxyl groups; zinc species.

Introduction

Methane (CH_4) is the main component of natural gas and the most important greenhouse gas. Despite to be promising feedstock for the chemical industry, methane is still mainly used as fuel for heat and power generation, which coincides with a major emission of CO_2[1,2]. For this reason valorization of methane into platform molecules is attractive from both economic and environmental aspects. The oxidation of methane into oxygenated products such as methanol is a very important process, and it has received extensive attention in industry and academia.[3–5] However, it remains a great challenge to realize the selective valorization of methane under mild conditions due to the inherently small polarizability (2.84×10^{-40} C^2m^2 J^{-1}) and high dissociation energy of C-H bond (440 kJ mol^{-1}) in CH_4 as well as the higher reactivity of target oxygenates. The selective hydroxylation of methane with high selectivity under mild conditions, achieved through the design of efficient catalysts, are considered a "holy grail" challenge in the field of catalysis.

As a promising green strategy, photocatalysis is widely used for converting solar light into chemical energy, and it may enable activation of C–H bonds in methane under mild conditions [6,7]. Recently, strategies combining metal-oxide based semiconductor and its supported nano or single-atom catalysts (SACs) and the use or in situ production of highly efficient oxidants such as $^{\bullet}OH$ have been proposed to accelerate photocatalytic methane activation in the gas–liquid–solid phase mode [8,9]. However, there is a trade-off effect between methane activation and oxygenate selectivity on photocatalysts for the methane oxidation, which can be caused by the excessive amount oxidant of $^{\bullet}OH$. Considerable endeavours have been made to overcome the problem of over-oxidation, including the modulation of catalyst band structures avoids oxidation of water to $^{\bullet}OH$ by valence band holes and introducing metal sites to transfer electrons to reduce O_2 to mild oxidant of $^{\bullet}O_2^-$ or $^{\bullet}OOH$. In addition to supplementary oxidant sources, the metal–OH group on the photocatalyst surface has been demonstrated to be capable of promoting the dehydrogenation of CH_4 by the formed of $^{\bullet}OH$, which could provide a hydrophilic reaction field for the activation of CH_4[10]. Nevertheless, the role of metal–OH group on photocatalyst also remains ambiguous due to the formation of metal-oxygen species (M-O) on metal-oxide photocatalyst that are also effective for methane conversion. Thus, it remains a major challenge to simultaneously clarify the role of surface –OH group on photocatalyst and to achieve high activity for photocatalytic methane conversion.

Recently, Zn-based materials have been explored as photocatalysts for the conversion of methane under mild conditions.[11] In light of the possibility that zinc ions may play an important role in methane activation, recent studies on Zn species incorporated into zeolites were performed.[12] Zeolite can provide a unique structure and microenvironment to modify the coordinated and electronic structure of metal species, making them particularly beneficial for the oxidation of methane. For example, Zn ions introduced into ZSM-5 zeolite exhibited remarkable light-absorption capabilities and demonstrated exceptional photocatalytic efficiency in the conversion of methane.[13] Chen and co-workers demonstrated that Zn^+-modified ZSM-5 zeolite catalyst exhibits photocatalytic activity for methane conversion at room temperature under the irradiation of ultraviolet (UV) light. However, upon irradiation with visible light, the photocatalytic activity was gradually reduced, and no activity was observed. Furthermore, the photocatalytic activities of the Zn-Beta and Zn-Y zeolites are lower than those of Zn-ZSM-5 zeolite, suggesting that the framework structure of the zeolite also affect the photocatalytic conversion of methane.[14] Based on the above study, it can be found that Zn^{2+} cation with an empty 4s orbital dispersed on zeolite is capable of accepting a photogenerated electron under light irradiation and be reduced to Zn^+. The generated Zn^+ on surfaces of zeolite works for the activation of C-H bond of CH_4, forming Zn-H-CH_3[14] or Zn-CH_3-H intermediates [15] which are key precursor intermediates for generating oxygenated liquid products in direct CH_4 oxidation. Besides, the formation of hydroxyl radicals (OH) on the photocatalyst surface has also been demonstrated to be capable of promoting the

dehydrogenation of CH_4 and the –OH groups that could provide a hydrophilic reaction field for promoting the activation of CH_4.[8,9] Despite the importance of hydroxyl groups in methane conversion, the role of surface hydroxyl groups present in zeolites on photocatalytic performance is briefly discussed[10,16].

Herein, we employed nanosized pure silica MFI zeolite (silicalite-1) to investigate the impact of hydroxyl groups (-OH) in promoting the activation of CH_4 under mild conditions. The use of silicalite-1 is due to its advantages such as well-defined structure, excellent hydrothermal stability, large surface area, and high density of Si-OH group, which could act as the platform for the study of OH group photocatalytic methane hydroxylation[14]. Taking advantage of the use of adequate synthesis protocol for the use of OH group,[11] we effectively introduce Zn into zeolite and show the impact of Zn atoms incorporated into framework for conversion of methane. The introduction of Zn heals most of the isolated external and internal silanol groups and silanol nests in the MFI zeolite structure resulting in a decrease in the yield of methanol. Structural and chemical properties of the isolated Zn sites are illustrated by various characterizations, revealing that the -OH groups are particularly beneficial for photocatalytic oxidation of methane.

Results and Discussion

The synthesis of nanosized pure silica MFI zeolite and metal-containing MFI zeolite has been explored in our group[17,19,20] In the present study, nanosized MFI zeolite (sample Si-MFI) was synthesized by following the procedures described previously[17]. The incorporation of different content of Zn in the zeolite sample was carried out by following two procedures: (i) One-Pot Synthesis (samples named as ZnX-MFI-O) and (ii) Incipient Wetness Impregnation (samples named as ZnX-MFI-IWI); X corresponds to the amount of Zn present in the samples. The Zn content of both series of ZnX-MFI-IWI and ZnX-MFI-O catalysts measured by ICP were 1.1, 2.2 and 5.4 wt.% (Table S1). The crystal structure of the catalysts was analysed by X-ray diffraction (Figure 1 and Figure S1). The XRD pattern of the Si-MFI sample shows features typical of well-crystalline silicalite-1 zeolite. Only Bragg peaks corresponding to MFI type structure are present in the of Zn2.2-MFI-IWI and Zn2.2-MFI-O samples (Figure 1). No zinc oxide phases were identified in the diffractograms, which was also supported by a UV-Vis analysis (Figure S2), suggest that the zinc species are homogeneously dispersed within the micropores of the zeolite samples. In addition, the XRD patterns display distinct broad diffraction peaks, typical for nanosized MFI zeolite crystals[18]. The XRD patterns of the samples presented in the range of 22−25° 2θ (Figure 1, inset) show a split of the peaks at ~23.3, 23.8, and 24.5° into two peaks for samples Zn2.2-MFI-O. This split indicates the space group transformation from orthorhombic Pnma (Si-MFI and Zn2.2-MFI-IWI) to monoclinic P21/c (Zn2.2-MFI-O). The transition from orthorhombic to monoclinic symmetry has already been observed after the insertion of Cu, W, and Mo into MFI zeolite framework[17,19,20]. This observation suggests the successful incorporation of Zn species into the framework of Zn-containing MFI zeolite prepared by One-Pot Synthesis in contrast to the samples prepared by IWI approach. Further, the N_2 adsorption–desorption isotherms (Figure 2) show a typical type I with a hysteresis loop, which is characteristic of microporosity over Zn-containing MFI zeolites prepared by One-Pot synthesis, while a combination of type I and type IV with a narrow H1 hysteresis loop for the sample Zn5.4-MFI-IWI (Figure S3), which is characteristic of microporosity and limited mesoporosity, The corresponding calculated textural parameters of the samples are summarized in Table S1, where a clear decrease in the BET specific surface areas and micropore volumes are observed with the increase in Zn content.

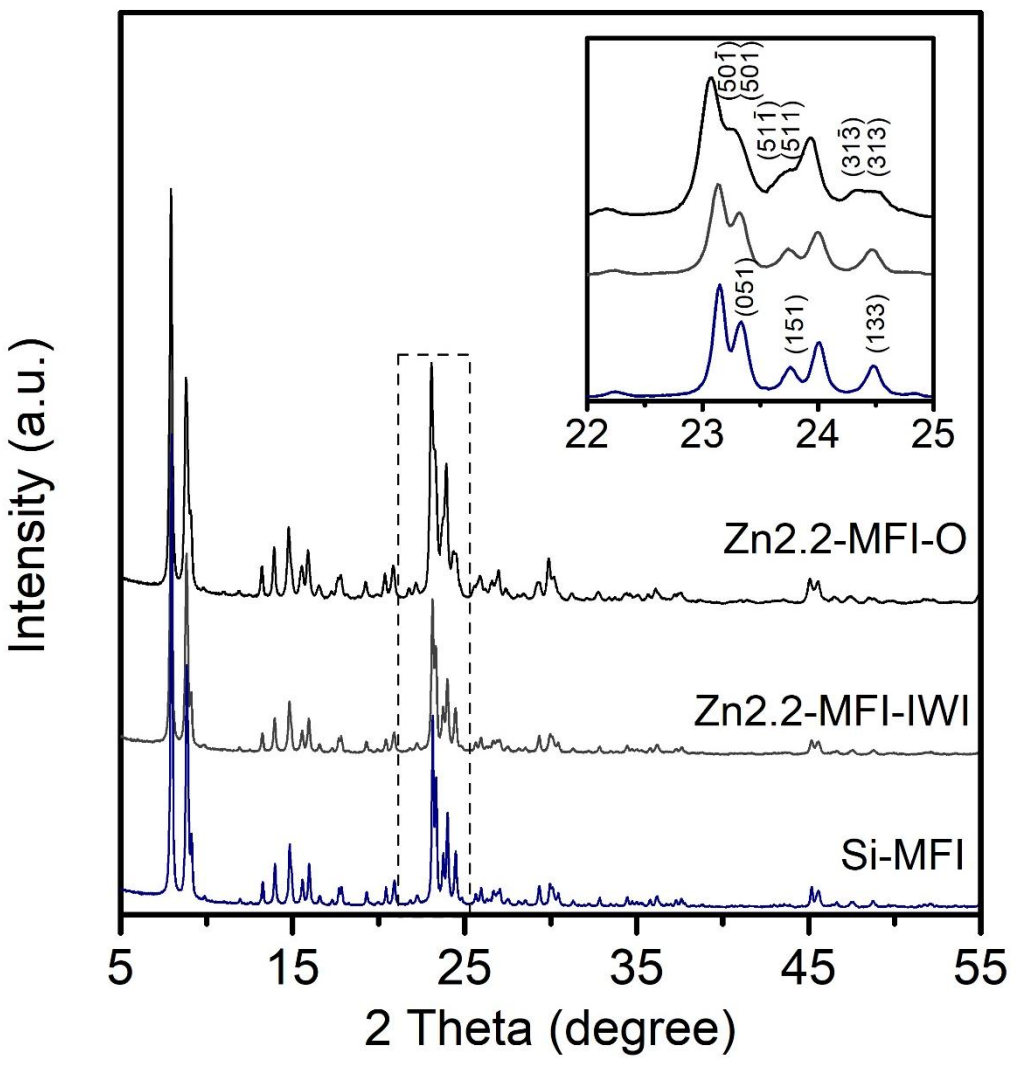

Figure 1. XRD patterns of pure Si-MFI, Zn2.2-MFI-O and Zn2.2-MFI-IWI catalysts; *Inset:* 22 – 25° 2Theta region.

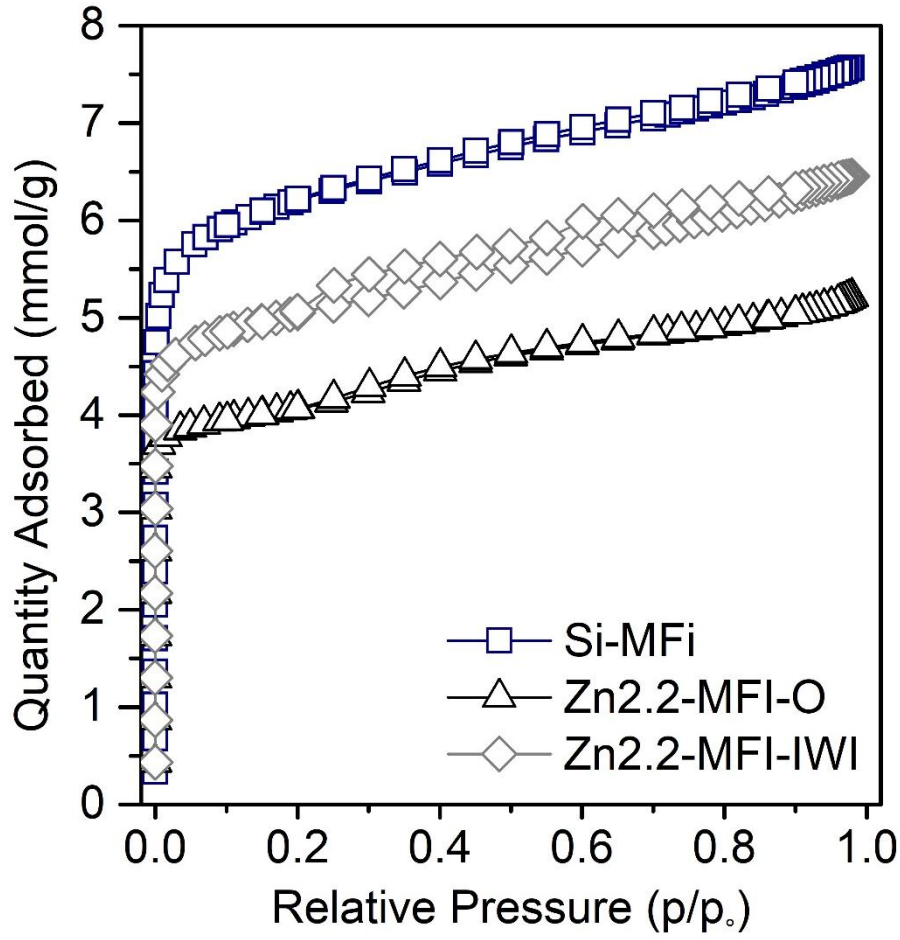

Figure 2. Nitrogen physisorption isotherms of pure silica Si-MFI and Zn-based zeolite catalysts: Zn2.2-MFI-O and Zn2.2-MFI-IWI.

The morphology of the particles was investigated using scanning electron microscopy (Figure 3). SEM images show that Si-MFI and Zn2.2-MFI-IWI particles are irregular spheres in shape with particle sizes around 100 nm (Figure S4a). The Zn2.2-MFI-O sample exhibits a more pronounced ellipsoid morphology with intergrowth of two different orientations (tweens) and an average particle size of 145 nm (Figure 2c). Indeed, the dynamic light scattering (DLS) data show an increase in the hydrodynamic size of the Zn-containing MFI zeolite prepared by One-Pot synthesis as the zinc content increases (Figures S5, Table S1). SEM images are in a good accordance with the DLS data and showed big spherically shaped particles for Zn-containing MFI zeolite containing the highest zinc content (Figure S4b). The distribution of zinc in the Zn-containing MFI samples was investigated by energy-dispersive X-ray spectroscopy (EDS, Figure 3). Both Zn2.2-MFI-IWI and Zn2.2-MFI-O samples show a homogeneous distribution of Zn with a mean content of 1.9 and 2.1 wt.%, respectively.

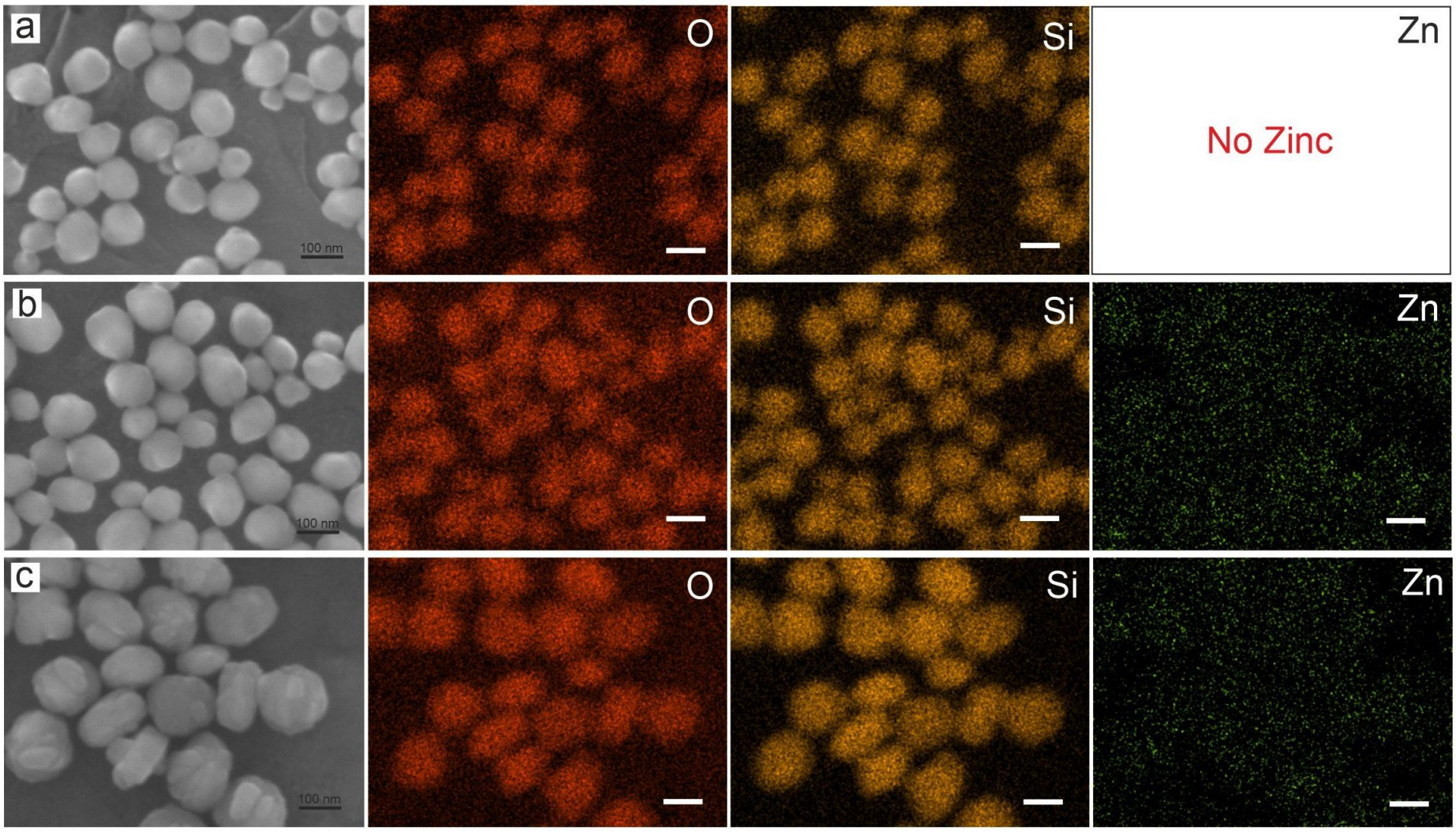

Figure 3. SEM images and the corresponding EDS elemental maps of (a) Si-MFI, (b) Zn2.2-MFI-IWI and (c) Zn2.2-MFI-O catalysts.

The content of hydroxyl groups in Si-MFI and Zn-containing MFI zeolite samples were studied by Fourier transform infrared (FTIR) spectroscopy (Figure 4a, Figure S6). As for Si-MFI, two absorption bands appear at 3745 and 3520 cm^{-1}, which are assigned to both isolated external and internal silanol groups and silanol nests, respectively[21]. No significant change is observed

after the introduction of Zn in the samples by Incipient Wetness Impregnation. However, the band at 3520 cm^{-1} completely disappears, whereas the intensity of the band at 3745 cm^{-1} decreases significantly in the sample Zn2.2-MFI-O. The absence of silanol nests band and decrease intensity of the band at 3745 cm^{-1} in the IR spectra of Zn-containing MFI zeolites Zn2.2-MFI-O prepared by One-Pot synthesis suggest that they are free of silanol defects, suggesting that the Zn^{2+} species may enter the 'T' vacancy[18]. The acidity of pure Si-MFI and the samples Zn2.2-MFI-IWI and Zn2.2-MFI-O characterized by pyridine adsorption/desorption FTIR spectroscopy shows that only Lewis acid sites with prominent bands at 1453, 1490, and 1610 cm^{-1} are detected (Figure 4b). These results indicate that Zn incorporated into the MFI zeolite framework can only generate Lewis, which are not capable of protonating pyridine. Pyridine adsorbed on Brønsted acid sites generally gives rise to the FTIR bands at 1440 and 1550 cm^{-1}, all absent in samples Zn2.2-MFI-O and Zn2.2-MFI-IWI (Figure 4b)[17,22].

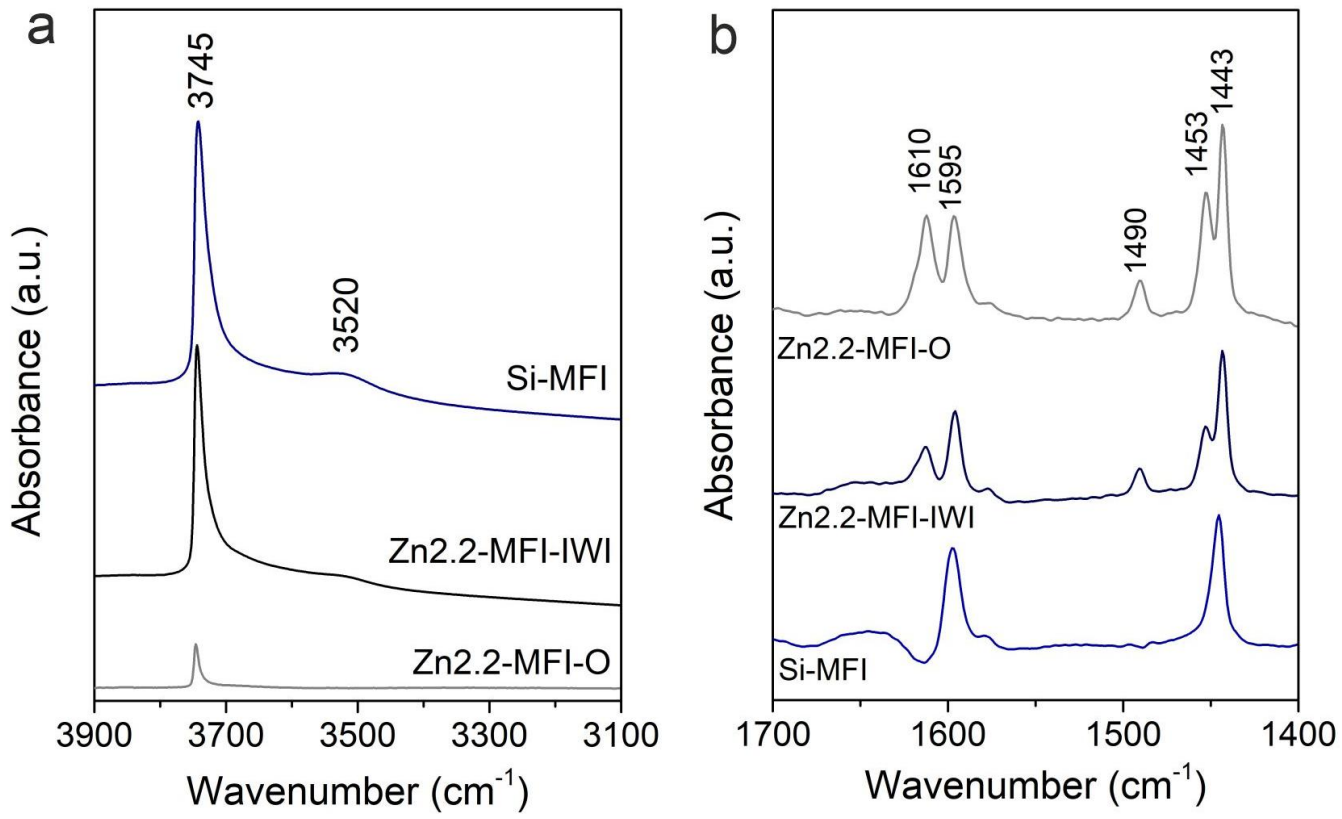

Figure 4. FTIR spectra of (a) OH region and (b) after pyridine adsorption of Si-MFI, Zn2.2-MFI-O and Zn2.2-MFI-IWI samples.

The healing of defects through the insertion of Zn by using One-Pot synthesis was further confirmed by means of ^{29}Si NMR spectroscopy. ^{29}Si NMR spectra of samples are shown in Figure 5a. The parent Si-MFI and Zn2.2-MFI-IWI samples present a low-resolution Q4 signal, which is also typical of the presence of silanol defects in the framework structure. After the introduction of Zn atoms by One-Pot synthesis in sample Zn2.2-MFI-O, a remarkable increase in the homogeneity of the structures is evidenced through the high resolution of the peaks at −117 ppm and −105 ppm attributed to $Si(OSi)_4$ (Q^4) species[19]. Through ^{29}Si NMR we can also confirm the hypothesis raised previously about the fact that Zn is not solely responsible for healing silanols, since the Zn2.2-MFI-IWI sample displays a low resolved Q^4 signal as Si-MFI, suggesting it has a low Zn incorporation into the zeolite framework. This further indicates that Zn has successfully occupied the silanol nest in sample Zn2.2-MFI-O. This observation is in a good agreement with the FTIR data (Figure 4a). X-ray photoelectron spectroscopy (XPS) was conducted to further investigate the composition and chemical state of the elements in samples Si-MFI, Zn2.2-MFI-O and Zn2.2-MFI-IWI (Figure 5b, Figure S7). The reference level to which all spectra were adjusted by a common shift of binding energies (BEs) to each was chosen to be the C 1s emission (284.6 eV). Si-MFI zeolite is composed of Si and O (Figure S7a). As can be seen from the survey spectra of samples Zn2.2-MFI-O and Zn2.2-MFI-IWI, two peaks corresponding to Zn 2p3/2 and Zn 2p1/2 (Figure 5b, Figure S7a) indicating the presence of zinc in both samples are observed. A spin-orbit splitting of ~23.0 eV in both cases confirms the presence of Zn as Zn^{2+} [23]. The binding energies of Zn 2p3/2 and Zn 2p1/2 at 1022.30 eV and 1045.32 eV, respectively for sample Zn2.2-MFI-IWI are measured. Compared with Zn2.2-MFI-IWI, a negative shift of 0.49 and 0.45 eV for the Zn 2p3/2 and Zn 2p1/2 peaks, respectively, for sample Zn2.2-MFI-O is observed (Figure 5b). Previously, the peaks at higher binding energy suggest the presence of zinc species having a tighter interaction with the zeolite framework[24–26]. Tamiyakul, et al.[27] reported that Zn^{2+} species localized at the cation exchanged sites have a high BE because they are present within an oxygen-deficient environment. Therefore, based on the XPS results, we could assume that isolated ZnO_x and/or $Zn(OH)^+$ species are anchored to the zeolite through the lattice oxygen for the Zn-containing zeolite prepared by Incipient Wetness Impregnation (Zn2.2-MFI-IWI), while the existence of a strong interaction between Zn^{2+} and the MFI framework is present in the Zn-containing MFI zeolite prepared by One-Pot synthesis (sample Zn2.2-MFI-O). Si and O are main elements whose BEs are not expected to change upon substitutions by smaller amounts of zinc as shown in Figure S7b,c.

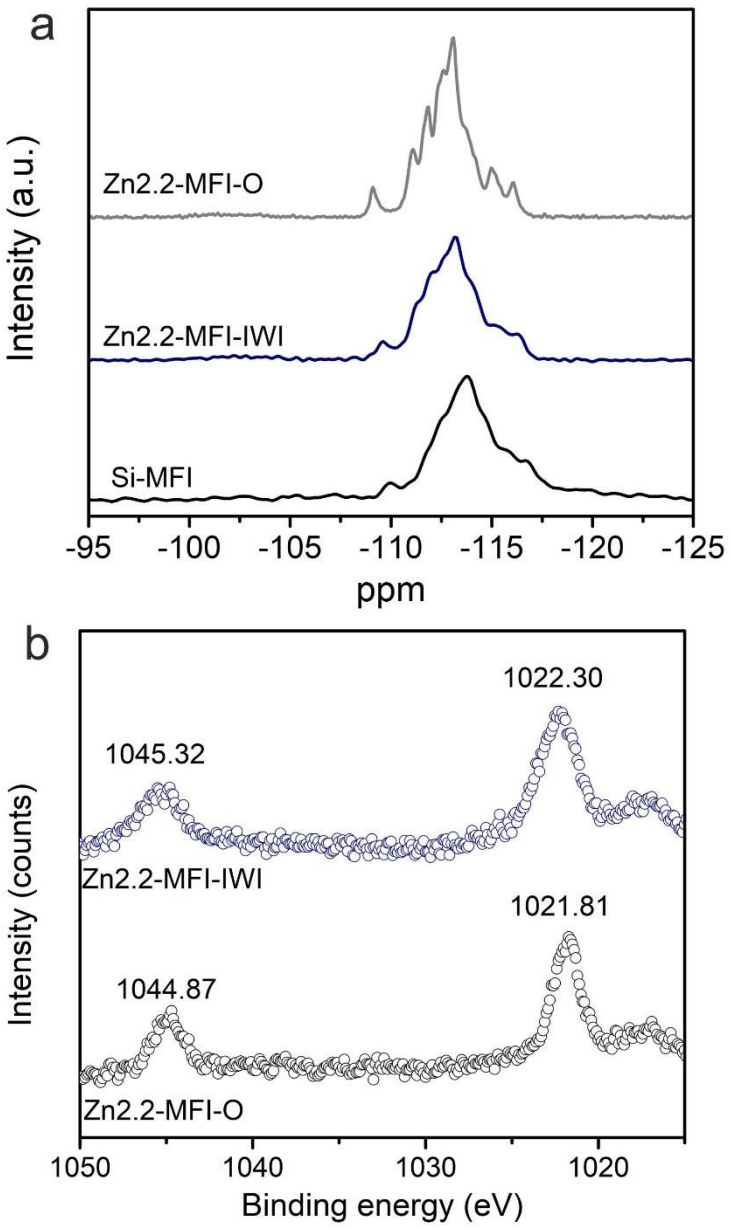

Figure 5. (a) ^{29}Si NMR spectra Si-MFI, Zn2.2-MFI-O and Zn2.2-MFI-IWI samples and (b) XPS Zn 2p core-level spectra of Zn2.2-MFI-O and Zn2.2-MFI-IWI samples.

The use of adequate synthesis protocol demonstrated be determinant to promoted the incorporation of atomically dispersed zinc atoms into the framework of nanosized MFI zeolite. The Zn2.2-MFI-O was found to have the space group of monoclinic phase (Figure 1) and contain low amount of silanol groups (Figure 4a). On the contrary, when Incipient Wetness Impregnation was used to prepare the Zn-containing MFI zeolite, the zinc species in the corresponding sample (Zn2.2-MFI-IWI) only present in the form of extra framework ZnO_x and/or $Zn(OH)^+$ species, and no phase transition is observed (Figure 1).

Photocatalyst tests

The photocatalytic CH_4 conversion was performed in a batch photoreactor at 20 °C using a 500 W Hg−Xe lamp as a light source. The liquid products were quantified by ^{1}H NMR (Figure S8), and the gas components were analyzed by gas chromatograph (GC) equipped with a thermal conductive detector (TCD) and a flame-ionized detector (FID) (Figure S9). As shown in Figure 6a, under aerobic conditions, the Si-MFI sample catalytically transforms CH_4 to C1 oxygenates such as CH_3OH, CH_3OOH and HCHO (1554.6 $\mu mol^{-1}\ g_{cat}^{-1}\ h^{-1}$) and C_2H_6 (101.9 $\mu mol^{-1}\ g_{cat}^{-1}\ h^{-1}$), with the selectivity of 43.8% taking into account all carbon-containing products. While for sample Zn2.2-MFI-IWI, the selectivity of C1 oxygenates and C_2H_6 on Zn2.2-MFI-O increases to 60.4%. With the increase of Zn loading in the catalysts from 1.1 to 5.4 wt%, the selectivity of C1 oxygenates and C_2H_6 shows an increase from 56.5% to 62.4% (Figure S10). The higher selectivity for sample Zn2.2-MFI-O result from the reduced surface OH group concentration as shown above (Figure 4a), which can further prevent the overoxidation of target products[28]. However, upon continuously increasing the Zn amount to 5.4 wt% (sample Zn5.4-MFI-O, Figure S10), the productivity of oxygenate and C_2H_6 decreases to 1043.7 $\mu mol^{-1}\ g_{cat}^{-1}\ h^{-1}$. The reasons can be ascribed that the enhanced incorporation of Zn species into the framework reducing the amount of OH group, thereby largely limiting the photocatalytic efficiency.

To investigate the reaction mechanism on the photocatalytic methane oxidation, some comparative experiments were conducted. As shown in Figure S11, there is no oxygenate product under N_2 atmosphere. However, upon introducing CH_4, a certain amount of carbon-containing products were observed, although this amount was significantly lower than that obtained when both air and CH_4 were introduced simultaneously. Furthermore, control experiments conducted without Si-MFI or light irradiation showed no detectable products, indicating that both Si-MFI and light exposure are essential for photocatalytic CH_4 conversion. Based on these observations, a photocatalytic CH_4 conversion pathway using the Si-MFI catalyst is proposed that is based on silanol OH- assisted mechanism (Figure 6b). Using the absorbed light energy, the Si-MFI catalyst is excited to generate conduction band electrons and valence band holes. The holes in the valence band of Si-MFI oxidize CH_4 into H^+ and $^{\cdot}CH_3$ (step 1), which then react with surface silanol OH groups to form CH_3OH product (step 2). Meanwhile, the left electrons from the conduction band of Si-MFI are subsequently injected into O_2 to produce H_2O_2 with H^+ through a reduction process (step 3). The H_2O_2 molecule generate $^{\cdot}OH$ and

OH^- (step 4), which adsorb onto unsaturated Si sites to regenerate the Si-OH group (step 5), ensuring the continuous photocatalytic hydroxylation of CH_4.

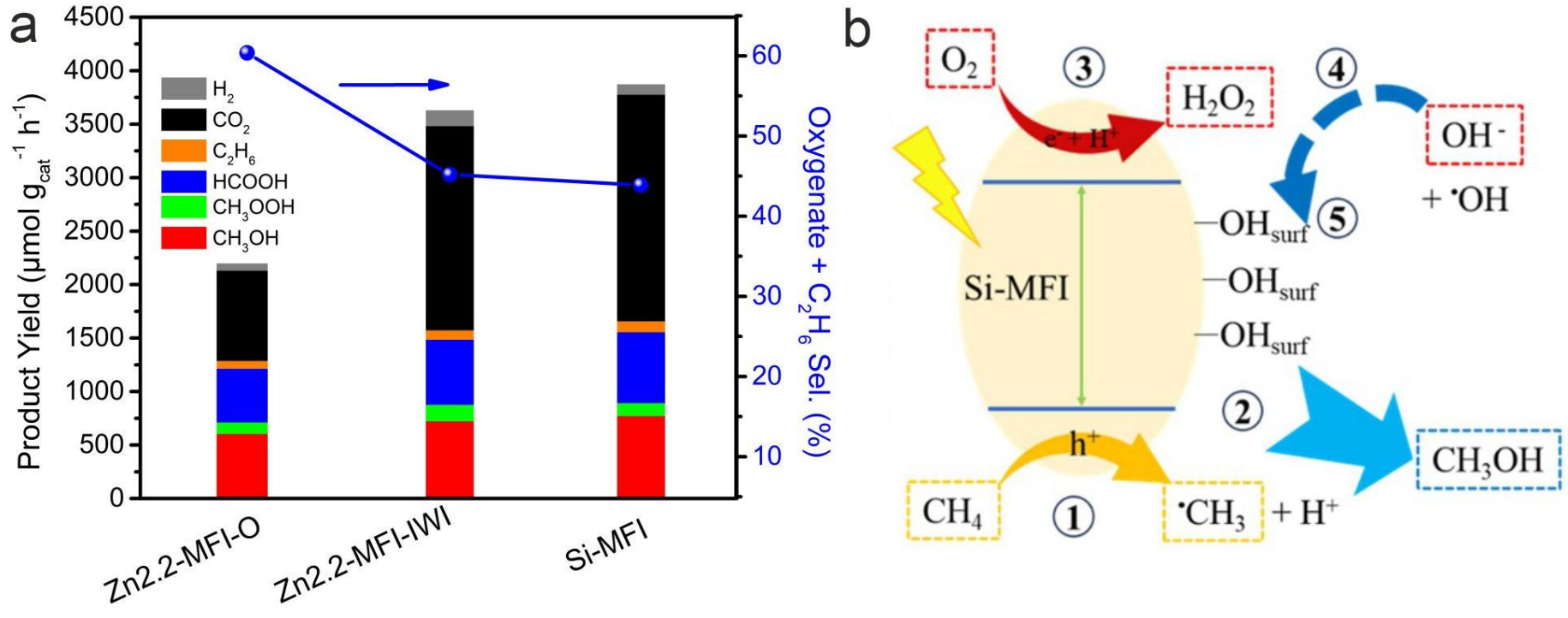

Figure 6. (a) Photocatalytic methane oxidation performance of pure silica Si-MFI and Zn-containing MFI zeolite samples: Zn2.2-MFI-O and Zn2.2-MFI-IWI and (b) proposed mechanism of photocatalytic methane oxidation on pure silica Si-MFI zeolite.

Conclusions

In summary, Zn-containing MFI zeolites with different zinc content have been synthesized using two procedures: One-Pot Synthesis and Incipient Wetness Impregnation. It is confirmed that Zn^{2+} atoms are incorporated into the framework successfully over Zn-containing MFI zeolite prepared by One-Pot synthesis approach, which is different from samples prepared by incipient wetness impregnation with mainly extra-framework $Zn(OH)^+$ species. The substitution of framework Si by Zn significantly reduces the silanol content, making the resulting zeolite highly hydrophobic. In addition, the insertion of Zn into the MFI structure induces a symmetry lowering, from orthorhombic (Pnma) to monoclinic (P21/n) typical of high silica MFI. Py-FTIR characterization indicate that Zn atoms embedded into the zeolite framework generate Lewis acid.

The selectivity of C1 oxygenates and C_2H_6 is higher for samples prepared by One-Pot synthesis approach than the sample prepared by Incipient Wetness Impregnation loaded with the same amount of Zn (Zn2.2-MFI-O > Zn2.2-MFI-IWI). The modification of the surface of nanosized-MFI zeolite by introduction of Zn into the framework (samples ZnX-MFI-O) leads to a decrease of the productivity of oxygenates and C_2H_6.This effect is attributed to the decrease of a hydroxyl groups which largely is limiting the photocatalytic efficiency. This work provides an alternative for exploration of zeolite catalyst with various amount of silanol defects for photocatalytic conversion of methane.

Experimental Section

Chemicals and materials

Tetraethylorthosilicate (TEOS, Sigma Aldrich, > 98%), tetrapropylammonium hydroxide solution (TPAOH, 20 wt% in water solution, Alfa Aesar), zinc nitrate hexahydrate ($Zn(NO)_3{\cdot}6H_2O$, Alfa Aesar, > 99%) and sodium hydroxide (NaOH, > 98%) used without further purification. Deionized (DI) water (Milli-Q) was used during the synthesis.

Synthesis of silicalite-1 zeolite (sample Si-MFI)

Silicalite-1 zeolite with an initial molar composition of $1.0SiO_2 : 0.12(TPA)_2O : 20H_2O$ was synthesized under static hydrothermal conditions. Typically, 5.85 g of TPAOH solution and 3.95 g of DI water were first mixed in polypropylene bottles and stirred for 30 min, and then 5 g of TEOS was added to the mixture dropwise. The mixture was stirred for 1 h and then aged for 18 h at room temperature in an orbital shaker. The obtained clear suspension was transferred to an oven and maintained at 90 °C for 48 h. The obtained solid was centrifuged, washed several times with DI water, freeze dried, and calcined at 550 °C for 5 h in air to remove the template (TPA^+).

Synthesis of zinc-containing MFI zeolites

Zn containing-MFI zeolites with different Zn content were synthesized by One-Pot Synthesis with an initial molar composition of $1.0SiO_2 : 0.12(TPA)_2O : aZnO{:}NaOH : 20H_2O$ (a = 0.012, 0.024, and 0.058). Typically, 5.85 g of TPAOH solution and 3.95 g of DI water were first mixed in polypropylene bottles and stirred for 30 min, and then the sodium zincate solution (2 M) was added to the mixture and stirred continuously for 1 h. Finally, 5 g of TEOS was added dropwise and the mixture was stirred for 1 h and then aged for 18 h at room temperature in an orbital shaker. The obtained clear suspension was transferred in an oven at 90 °C for 48 h under static hydrothermal conditions. The obtained solid was centrifuged, washed several times with DI water, freeze dried, and calcined at 550 °C for 5 h in air. The calcined samples in sodium form were transformed into acidic form by treatment with NH_4NO_3 solution and calcination at 550 °C for 5h. The samples were denoted as ZnX-MFI-O, where X is the Zn content.

Zn-containing MFI zeolite was also prepared by Incipient Wetness Impregnation (ZnX-MFI-IWI, where X is the zinc content). Typically, $Zn(NO_3)_2{\cdot}6H_2O$ was dissolved in DI water and mixed with the pure silica Si-MFI zeolite. The impregnated zeolite was dried at 60 °C overnight and calcined at 550 °C for 5h.

Characterization

The samples were characterized by powder X-ray diffraction (PXRD) using a XRDynamic 500 diffractometer (Anton Paar) with Cu Kα radiation (λ = 1.54059 Å), operating at 40 kV and 40 mA. The chemical composition of samples was analysed by inductively coupled plasma mass spectrometry (ICP-MS) using a 7900 ICP-MS from Agilent Technologies. Dynamic Light Scattering (DLS) experiments were conducted on a Malvern Zetasizer Nano instrument equipped with a backscattering geometry (a scattering angle of 173°, He–Ne laser with a wavelength of 632.8 nm. Scanning Electron Microscopy (SEM) images and energy dispersive X-ray spectroscopy (EDS) analyses were performed using a JEOL JSM-IT800 Schottky field emission scanning electron microscope in high-vacuum mode (pressure $<10^{-4}$ Pa). SEM images were collected using a low accelerating voltage of 0.8 keV and a current of 10 nA. EDS elemental mapping analysis were acquired using an electron beam with a 5 keV accelerating voltage,current of 10 nA and a dwell time of 0.1 ms. N_2 sorption measurements were conducted on a Micromeritics ASAP2020 volumetric adsorption analyser. Before the measurement, the 0.1 g sample was degassed at 350 °C under a vacuum for 6 h. Then the sample was cooled down to room temperature and tested in liquid N_2 (−196 °C). The total surface area was evaluated based on the Brunauer-Emmett-Teller (BET) equation. The micropore surface area and micropore volume were calculated using the t-plot method. Fourier transform infrared (FTIR) spectra were obtained using a Nicolet Magna 550-FT-IR spectrometer. 20 mg of samples were pressed into a self-supporting pellet and placed into a quartz cell. Prior to the acquisition of FTIR spectra, pellets were pre-treated at 450 °C for 3h under vacuum (< 10^{-5} Torr). All spectra were recorded at 128 scans and a resolution of 4 cm^{-1}. Ultraviolet−visible spectrophotometer (UV−vis) spectra were detected at room temperature using Varian Cary 4000 UV–vis spectrometer. Fourier transform infrared spectra of pyridine (Py-FTIR) analysis were recorded by a Nicolet Magna 550-FT-IR spectrometer (4 cm^{-1} optical resolution). The 20 mg samples were pressed into a self-supporting disc and placed into a quartz cell. Afterward, the samples were pre-treated at 450 °C for 3h under vacuum (2.5 ×10^{-6} Torr) and then cooled to room temperature. Subsequently, successive small doses pyridine was adsorbed at room temperature, followed by purging with vacuum for 20 min 150 °C to remove the physisorbed pyridine. The XPS spectra were taken using an ESCALAB 250Xi spectrometer, equipped with an aluminum monochromater for a 1486.6 eV source working at 120 W. The binding energies were corrected with respect to C 1s of 284.6 eV. ^{29}Si nuclear magnetic resonance (NMR) spectra were obtained on a 11.7 T Bruker Avance 500 spectrometer equipped with a 4 mm probe using a spinning frequency of 14 kHz.

Photocatalytic test reaction

The photocatalytic test reactions were performed in a 100 mL batch reactor, with a Mercury-Xenon arc lamp (Newport, 500 W) used as a light source. A quartz window is located on the top of the reactor, which enables the vertical transmission of the incident light. Prior to the reaction, 20 mg catalyst was homogeneously dispersed in 30 mL DI water via sonification and then transferred into the reactor. Afterwards, the reactor was evacuated by a vacuum pump and charged sequentially with Air and CH_4 to a designated pressure (32 bar, absolute pressure). Throughout the reaction, the catalyst-water suspension was magnetically stirred, and the reaction temperature was kept at 20 °C by a circulating water machine at a constant temperature. The irradiation time in each batch is varied from 1 to 2 h. After the photocatalytic reaction, gaseous products were analyzed by a gas chromatograph (PerkinElmer Clarus 580 GC) equipped with a PoraBOND Q and a ShinCarbon ST 100/120 columns, as well as with a thermal conductive detector and a flame ionized detector. The quantifications of C_2H_6, H_2 and CO_2 were based on the calibration curves (Figure S12). The liquid product was analyzed by ^1H nuclear magnetic resonance (NMR) spectroscopy, by mixing 0.5 mL filtered liquid sample with 0.1 mL DMSO/D_2O solution (1/2000, v/v, DMSO is the internal standard). The quantification of CH_3OH and formic acid was made based on the calibration curves (Figures S13). The amount of CH_3OOH was obtained with the same equation of CH_3OH.The selectivity of oxygenate and C_2H_6 was calculated based on the mole numbers of all liquid oxygenates. The selectivity (%) and yields (μmol g_{cat}^{-1} h^{-1}) of oxygenate and C_2H_6 were calculated using the following equations (1-2), respectively:

$$\text{Oxygenate and } C_2H_6 \text{ selectivity} = n_{(\text{Oxygenate and C2H6})}/n_{(\text{total products})} \times 100\% \quad (1)$$

$$\text{Product yield} = n_{(\text{product})}\, m_{cat.} \times t \quad (2)$$

Conflicts of interest

There are no conflicts to declare.

Acknowledgements

The authors gratefully acknowledge the support of the French National Research Agency: ANR PulseCoMeth project (ANR-22-CE050-0018). The support from the European Union (ERC, ZEOLIghT, 101054004) is acknowledged. The views and opinions expressed are, however, those of the author(s) only and do not necessarily reflect those of the European Union or the European Research Council. Neither the European Union nor the granting authority can be held responsible for them. Co-funding from the Region of Normandy (CLEAR) for the Centre for Zeolites and Nanoporous Materials is acknowledged

Author Contribution’s

Diógenes Honorato Piva and Svetlana Mintova conceived the research, analyzed and finalized the manuscript. Sajjad Ghojavand contributed to the NMR and FTIR tests. Francesco Dalena contributed to the Py-FTIR analysis. Vincent De Waele performed the

UV–vis measurement. Geqian Fang, Vitaly Ordomsky and Andrei Khodakov performed the photocatalytic test. Tiago Fernandes and Yury V. Kolen'ko assisted the XPS experiments.

References

1 P. Xie, J. Ding, Z. Yao, T. Pu, P. Zhang, Z. Huang, C. Wang, J. Zhang, N. Zecher-Freeman, H. Zong, D. Yuan, S. Deng, R. Shahbazian-Yassar, C. Wang, *Nat Commun* **2022**, *13*, 1375.

2 Z. Jin, L. Wang, E. Zuidema, K. Mondal, M. Zhang, J. Zhang, C. Wang, X. Meng, H. Yang, C. Mesters, F.-S. Xiao, *Science (1979)* **2020**, *367*, 193.

3 S. Bai, F. Liu, B. Huang, F. Li, H. Lin, T. Wu, M. Sun, J. Wu, Q. Shao, Y. Xu, X. Huang, *Nat Commun* **2020**, *11*, 954.

4 X. Wu, H. Zhang, S. Xie, Y. Wang, *Chem Catalysis* **2023**, *3*, 100437.

5 T. Shi, D. Sridhar, L. Zeng, A. Chen, *Electrochem commun* **2022**, *135*, 107220.

6 L. Yuliati, H. Yoshida, *Chem Soc Rev* **2008**, *37*, 1592.

7 M. Graetzel, K. R. Thampi, J. Kiwi, *J Phys Chem* **1989**, *93*, 4128.

8 K. Villa, S. Murcia-López, T. Andreu, J. R. Morante, *Catal Commun* **2015**, *58*, 200.

9 Q. Cheng, A. Wang, Z. Song, J. Bao, J. Xue, Y. Wei, S. Li, L. Lv, J. Ding, M. Cai, J. Chen, Q. Wang, C. Gao, S. Sun, *J Environ Chem Eng* **2021**, *9*, 105080.

10 F. Sastre, V. Fornés, A. Corma, H. García, *J Am Chem Soc* **2011**, *133*, 17257.

11 X. Meng, X. Cui, N. P. Rajan, L. Yu, D. Deng, X. Bao, *Chem* **2019**, *5*, 2296.

12 G. Chen, Y. Zhao, L. Shang, G. I. N. Waterhouse, X. Kang, L. Wu, C. Tung, T. Zhang, *Advanced Science* **2016**, *3*.

13 L. Li, G. Li, C. Yan, X. Mu, X. Pan, X. Zou, K. Wang, J. Chen, *Angewandte Chemie International Edition* **2011**, *50*, 8299.

14 L. Li, G. Li, C. Yan, X. Mu, X. Pan, X. Zou, K. Wang, J. Chen, *Angewandte Chemie International Edition* **2011**, *50*, 8299.

15 Y. Zhao, C. Cui, J. Han, H. Wang, X. Zhu, Q. Ge, *J Am Chem Soc* **2016**, *138*, 10191.

16 S. Murcia-López, M. C. Bacariza, K. Villa, J. M. Lopes, C. Henriques, J. R. Morante, T. Andreu, *ACS Catal* **2017**, *7*, 2878.

17 J. Grand, S. N. Talapaneni, A. Vicente, C. Fernandez, E. Dib, H. A. Aleksandrov, G. N. Vayssilov, R. Retoux, P. Boullay, J.-P. Gilson, V. Valtchev, S. Mintova, *Nat Mater* **2017**, *16*, 1010.

18 I. C. Medeiros-Costa, E. Dib, F. Dubray, S. Moldovan, J.-P. Gilson, J.-P. Dath, N. Nesterenko, H. A. Aleksandrov, G. N. Vayssilov, S. Mintova, *Inorg Chem* **2022**, *61*, 1418.

19 F. Dubray, S. Moldovan, C. Kouvatas, J. Grand, C. Aquino, N. Barrier, J.-P. Gilson, N. Nesterenko, D. Minoux, S. Mintova, *J Am Chem Soc* **2019**, *141*, 8689.

20 P. Peng, S. Moldovan, A. Vicente, V. Ruaux, M. Debost, H. Hu, H. A. Aleksandrov, G. N. Vayssilov, Z.-F. Yan, S. Mintova, *Microporous and Mesoporous Materials* **2023**, *357*, 112625.

21 A. Zecchina, S. Bordiga, G. Spoto, D. Scarano, G. Petrini, G. Leofanti, M. Padovan, C. O. Areàn, *J. Chem. Soc., Faraday Trans.* **1992**, *88*, 2959.

22 C. A. Emeis, *J Catal* **1993**, *141*, 347.

23 Z. Deng, M. Chen, G. Gu, L. Wu, *J Phys Chem B* **2008**, *112*, 16.

24 C. Song, X. Li, X. Zhu, S. Liu, F. Chen, F. Liu, L. Xu, *Appl Catal A Gen* **2016**, *519*, 48.

25 X. Niu, J. Gao, Q. Miao, M. Dong, G. Wang, W. Fan, Z. Qin, J. Wang, *Microporous and Mesoporous Materials* **2014**, *197*, 252.

26 R. A. Hunsicker, K. Klier, T. S. Gaffney, J. G. Kirner, *Chemistry of Materials* **2002**, *14*, 4807.

27 S. Tamiyakul, W. Ubolcharoen, D. N. Tungasmita, S. Jongpatiwut, *Catal Today* **2015**, *256*, 325.

28 Y. Sun, J. Miao, X. Fan, K. Zhang, T. Zhang, *Small Struct* **2024**.